J. Fluid Mech. (1992), *vol.* 240, *pp.* 355–377
Printed in Great Britain

An experiment on boundary mixing. Part 2 The slope dependence at small angles

By H. SALMUN† AND O. M. PHILLIPS
Department of Earth and Planetary Sciences, The Johns Hopkins University, Baltimore, MD 21218, USA

(Received 15 January 1990 and in revised form 4 February 1992)

Experiments of the type described by Phillips *et al.* (1986) were performed using different slopes with the aim of examining the slope dependence of the buoyancy and volume transports, particularly at small slopes. The new observations confirmed the general flow patterns described for experiments conducted at a fixed slope, but a reconsideration of the local balances suggest that the buoyancy flux at small slopes θ is proportional to $(\kappa N)^{\frac{3}{2}} \sin\theta$, where κ is the turbulent diffusivity, and the volume flux associated with the overall convergence flow is linear with depth and proportional to $(\kappa^{\frac{3}{2}}/N^{\frac{1}{2}}h)\sin\theta$, where h is the thickness of the pycnocline. These differ in their dependence on the slope suggested (but not tested) in Phillips *et al.*, and are generally consistent with measurements over a range of slopes from 7.1° to 23.5°.

1. Introduction

The oceans are generally stably stratified and limited laterally by sloping boundaries. The flow along these boundaries is usually turbulent; the turbulence may be generated by large-scale gravity currents or lateral currents, breaking of internal waves incident upon the boundaries, mean tidal flows or other mechanisms. Away from the bottom boundaries, turbulence decays so that we have a turbulent boundary-layer region bounding a much larger region of generally non-turbulent flow. A schematic diagram depicting this geometry and the flow patterns described below is provided in figure 1.

It was suggested as early as 1966 by Walter Munk that boundary mixing may contribute significantly to the overall vertical mixing in a stratified ocean, the largest cross-isopycnal mixing occurring in boundary mixed layers which are then advected into the interior. This hypothesis has been explored in several studies that include field observations (Wunsch 1972; Armi 1978; Gregg & Sanford 1980; and many others), laboratory experiments (Ivey & Corcos 1982; Thorpe 1982; Phillips, Shyu & Salmun 1986; Ivey 1987; and others), and theoretical analyses (Thorpe 1987; Garrett 1990; Woods 1991). Mixing at the boundaries may be the result of interactions between mean flows and the rough bottom or due to the reflection of internal waves. When these waves are reflected off sloping boundaries the vertical shear is enhanced, leading to possible shear flow instabilities and wave breaking, providing significant amounts of energy to drive the mixing (Cacchione & Wunsch 1974; Stigebrant 1976; Garrett 1979; Eriksen 1985; Ivey & Nokes 1989; and several others). Many other studies have also concentrated on the importance of boundary-

† Present address: Robert Hooke Institute, The Observatory, Clarendon Laboratory, Parks Road, Oxford OX1 3PU, UK.

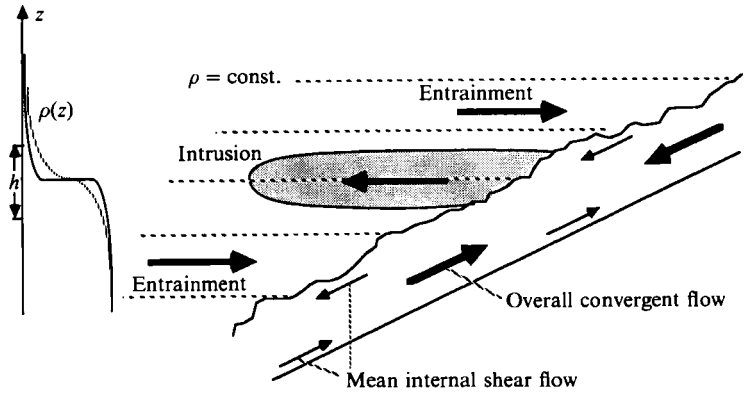

FIGURE 1. A schematic diagram of the flow inside the boundary layer and the stratified ambient regions.

layer mixing in accounting for the overall mixing observed in estuaries, lakes and fjords (Caldwell, Brubaker & Neal 1978; Marmorino, Danos & Maki 1980).

The first laboratory investigation to study the process of boundary mixing using a boundary of fixed uniform slope (9.4°) was undertaken by Phillips *et al.* (1986, hereinafter referred to as PSS), with the turbulent boundary layer along the slope being generated by an oscillatory mat. It was evident that in the boundary-layer region, the lateral mixing due to turbulence immediately causes a reduction in the gradients of salt in this layer, inducing a perturbation in the stratification of the fluid. Isopycnals cannot remain horizontal and hence horizontal variations of buoyancy occur. This implies that the fluid near the outer edge is denser than the fluid at the same level in the ambient surroundings and that the fluid near the bed is less dense than the outside fluid at this level. In response to these variations in the buoyancy field an internal circulation in the boundary layer develops whereby the fluid nearest the wall moves upwards while the fluid in the outer part of the boundary layer moves downwards, constituting one of the components of the mean flow in the turbulent boundary layer. The mean density in the boundary layer tends to become uniform in the direction normal to the slope and this tendency is accentuated as mixing proceeds.

This internal circulation enhances the dispersion of salt up and down the slope beyond that produced by turbulence alone, which results in the spreading of isopycnals in the slope direction beyond the extent of the original ambient stratification. Denser fluid is dispersed above the level of the ambient stratification and less dense fluid below, which induces an overall convergence flow along the slope with entrainment of outside fluid into the boundary layer at the top and bottom and by intrusion of mixed boundary fluid into the ambient stratified region.

The internal mean flow in the boundary layer has therefore two superimposed components: the internal counterflow streaming produced by the turbulent mixing across the layer and the net flow convergence along the slope that balances the dispersion along it. The resulting intrusion of boundary-layer fluid into the ambient regions will weaken the density gradients there so that the density stratification that surrounds the turbulent boundary layer gradually changes, affecting ultimately the flow inside the boundary layer as well as its growth. The layer of boundary-mixed fluid may then be carried away over large horizontal distances into the interior of the body of fluid, affecting in turn its properties far away from the boundary regions.

The basic requirement needed to establish the mechanism described above is a divergence of the turbulent density flux along the slope within the boundary layer. In general this density flux will vary along the boundary layer if the density gradients change with distance along the slope, as is the case when the stratification is non-uniform with depth, if the strength of the source of turbulence is not constant along the boundary as may be expected in the oceans, or if the angle of the sloping boundary changes significantly over short distances.

The early experiments were conducted at a single slope, while the stratification of the ambient fluid and the strength of mixing (characterized by the frequency and amplitude of the mat oscillations) were varied over as wide a range as possible. A simple scaling analysis was developed based essentially upon the diffusive laminar boundary layer in a uniformly stratified fluid with a sloping boundary (Phillips 1970). This provided a satisfactory collapse of measurements of the distributions of buoyancy and volume fluxes and also suggested how these fluxes and the boundary-layer thickness should vary with the angle of the slope. The original intent of the experiments to be described here was simply to check this slope dependence by rebuilding the apparatus several times to give different bed angles but it transpired that the fluxes measured at different slopes varied in a manner opposite to that described by the PSS scaling. At small slopes, the buoyancy and volume fluxes were expected to increase as the slope decreased but, as will be described later, they were found to decrease. It became evident that the scaling in PSS could not be pertinent when the bottom slope is small and that led to a revision of the model's equations, the assumptions used there, as well as the interpretations of the laboratory experiments. In the next section, the approach of PSS is revised for the limit of small slopes, after which the new measurements will be described.

2. The governing equations

Consider the turbulent boundary layer above a bed with constant slope θ with respect to the horizontal, outside which the ambient fluid is stratified with $\rho = \rho(Z)$ as in figure 2. When the internal timescales characteristic of the turbulence in the boundary layer are small compared to the characteristic timescales for the changes in both the ambient stratification and the flow generating the turbulence, then the mean flow in the turbulent boundary layer can be considered steady. Furthermore, when the mechanism generating the turbulence is uniform along the slope, the induced mean flow is two-dimensional in the (x, y)-plane of figure 2.

Suppose that the region of significant stratification in the ambient fluid extends over a vertical distance h, so that the distance up and down the slope over which the turbulent boundary layer modifies this stratification is $L \sim h/\sin\theta$. The boundary-layer thickness scale is represented by H so that the aspect ratio of the region is

$$\epsilon = \frac{H}{L} \sim \frac{H}{h}\sin\theta.$$

We are particularly interested in cases of relatively small slope so that $\epsilon \ll 1$ although H and h may be comparable. The sketch in figure 2 shows the coordinate systems of the ambient and boundary regions (X, Z) and (x, y) respectively. They are related by the coordinate transformation defined by

$$X = x\cos\theta - y\sin\theta, \quad Z = x\sin\theta + y\cos\theta.$$

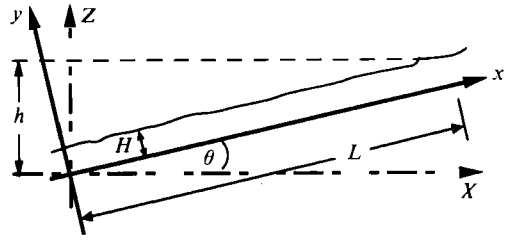

FIGURE 2. Definition of coordinate system.

For the turbulent flow the mean momentum equations reduce to

$$u\frac{\partial u}{\partial x}+v\frac{\partial u}{\partial y}=-\frac{1}{\rho_0}\frac{\partial p}{\partial x}-\frac{g\rho}{\rho_0}\sin\theta-\left(\frac{\partial}{\partial x}\overline{u'^2}+\frac{\partial}{\partial y}\overline{u'v'}\right), \tag{1}$$

in the direction of the slope, and in the normal direction

$$u\frac{\partial v}{\partial x}+v\frac{\partial v}{\partial y}=-\frac{1}{\rho_0}\frac{\partial p}{\partial y}-\frac{g\rho}{\rho_0}\cos\theta-\left(\frac{\partial}{\partial x}\overline{u'v'}+\frac{\partial}{\partial y}\overline{v'^2}\right), \tag{2}$$

where u, v, and u', v' represent the mean flow and turbulent fluctuations respectively, ρ and ρ_0 represent the mean density field and the reference density, and p is the mean pressure field. The mean buoyancy distribution in the boundary layer is governed by the following equation:

$$u\frac{\partial B}{\partial x}+v\frac{\partial B}{\partial y}=-\frac{\partial}{\partial x}\overline{u'b'}-\frac{\partial}{\partial y}\overline{v'b'}, \tag{3}$$

where $B=-g(\rho-\rho_0)/\rho_0$ and $b'=-g\rho'/\rho_0$ are the mean and fluctuating buoyancy fields respectively. The equations of motion are completed with the continuity equation $\nabla\cdot\boldsymbol{u}=0$, in virtue of which we can define the stream function ψ for the mean flow such that $u=\partial\psi/\partial y$ and $v=-\partial\psi/\partial x$.

We assume that the turbulent fluxes of momentum and buoyancy can be expressed in terms of an eddy viscosity $\nu(y)$ and an eddy diffusivity $\kappa(y)$. In the regions surrounding the boundary layer, referred to as ambient or interior regions, the stratified fluid is not turbulent and the flow there is in essence inviscid and non-diffusive so that $\nu(y),\kappa(y)=0$ when $y>H$. Very near the boundaries, the eddy coefficients are also small, frequently being assumed to be linear in y. An equation for the mean vorticity of the flow (in the axial or z-direction) is readily obtained by cross-differentiation of the momentum equations, yielding

$$u\frac{\partial\omega}{\partial x}+v\frac{\partial\omega}{\partial y}=\cos\theta\frac{\partial B}{\partial x}-\sin\theta\frac{\partial B}{\partial y}+\nu\nabla^2\omega+\left(\frac{\partial\omega}{\partial y}-\nabla^2 u\right)\frac{\partial\nu}{\partial y}-\frac{\partial^2\nu}{\partial y^2}\frac{\partial u}{\partial y} \tag{4}$$

where $\omega=-\nabla^2\psi$. The mean buoyancy equation, (3), can then be expressed as

$$u\frac{\partial B}{\partial x}+v\frac{\partial B}{\partial y}=\kappa\frac{\partial^2 B}{\partial x^2}+\frac{\partial}{\partial y}\left(\kappa\frac{\partial B}{\partial y}\right). \tag{5}$$

The ambient density field may have a variety of forms. When it varies linearly with depth, the equations simplify greatly and with appropriate specifications for $\nu(y)$ and $\kappa(y)$ they can be solved analytically (Thorpe 1987; Garrett 1990; Woods 1991). In the experiments, $\partial B/\partial Z=N^2$ is not constant, but has a single maximum.

The boundary-layer thickness and the distributions of $\nu(y)$ and $\kappa(y)$ are not known *a priori*, but the governing equations can be used to determine characteristic scales of motion in terms of which the experimental results are to be described.

We first concentrate attention on the vicinity of the level of maximum stratification where the ambient stability frequency, defined as usual by $N^2 = (-g/\rho_0)(\partial\rho/\partial Z)$, is locally equal to a constant. In this vicinity,

$$\frac{\partial B}{\partial x} = N^2 \sin\theta \tag{6}$$

and other derivatives along the layer are small because the turbulence is locally homogeneous in the x-direction (since the turbulent source is constant along the boundary). There then, (4) and (5) reduce to

$$0 = N^2 \cos\theta \sin\theta - \sin\theta \frac{\partial B}{\partial y} - \frac{\partial^2}{\partial y^2}\left(\nu(y)\frac{\partial^2 \psi}{\partial y^2}\right), \tag{7}$$

and

$$\frac{\partial \psi}{\partial y} N^2 \sin\theta = \frac{\partial}{\partial y}\left(\kappa(y)\frac{\partial B}{\partial y}\right), \tag{8}$$

respectively. These equations express the balances between the generation of vorticity by the horizontal gradient of buoyancy and turbulent diffusion, and between the divergence of the turbulent flux normal to the boundary and advective buoyancy flux along the slope. The second may be integrated in the y-direction and with $\psi = 0$ and $\overline{b'v'} = -\kappa(y)\,\partial B/\partial y = 0$ on $y = 0$, we have

$$N^2 \sin\theta \psi(y) = \kappa(y)\frac{\partial B}{\partial y}. \tag{9}$$

Since the turbulent buoyancy flux vanishes outside the layer, $\psi = 0$ when $y \to H$; the boundary layer in this vicinity has zero net volume flux. Hence, the flow in the boundary layer described locally by these equations is entirely made up of the lateral shear flow component due to the turbulent mixing normal to the slope.

The total upslope buoyancy flux may be found by adding the diffusive flux and advective fluxes, i.e.

$$F_B = F_B^{\text{diff}} + F_B^{\text{adv}} = \int_0^\delta \left[-\kappa(y)\frac{\partial B}{\partial x} + B\frac{\partial \psi}{\partial y}\right] dy. \tag{10}$$

The advective buoyancy flux along the layer

$$\int_0^\delta B\frac{\partial \psi}{\partial y}\,dy = -\int_0^\delta \psi \frac{\partial B}{\partial y}\,dy = -\int_0^\delta \kappa(y)\left(\frac{\partial B}{\partial y}\right)^2 (N^2 \sin\theta)^{-1}\,dy \tag{11}$$

from (9). The total upslope buoyancy flux is then

$$F_B = -\int_0^\delta \kappa(y)\left[N^2 \sin\theta + \left(\frac{\partial B}{\partial y}\right)^2 (N^2 \sin\theta)^{-1}\right] dy, \tag{12}$$

an elegant result due to Garrett (1990). Alternatively

$$F_B = -\int_0^\delta N^2 \sin\theta \left[\kappa(y) + \frac{\psi^2(y)}{\kappa(y)}\right] dy. \tag{13}$$

Equations (7) and (9) can be combined into a single equation for the mean stream function, i.e.

$$\frac{\partial^2}{\partial y^2}\left[\nu(y)\frac{\partial^2\psi}{\partial y^2}\right]+\frac{N^2\sin^2\theta}{\kappa(y)}\psi(y)=N^2\cos\theta\sin\theta, \tag{14}$$

the terms of which arise respectively from the diffusion of mean vorticity and the generation of it by buoyancy gradients normal to and parallel to the sloping boundary. PSS assumed that all three terms in (14) are comparable in magnitude so that if ψ_s represents the scale for the stream function distribution and ν, κ the scale values of $\nu(y), \kappa(y)$ in the layer, then

$$\nu\frac{\psi_s}{H^4}\sim\frac{N^2\sin^2\theta\psi_s}{\kappa}\sim N^2\cos\theta\sin\theta, \tag{15}$$

which leads to

$$H\sim\left(\frac{\nu\kappa}{N^2\sin^2\theta}\right)^{\frac{1}{4}} \tag{16}$$

and

$$\psi_s\sim\kappa\cot\theta. \tag{17}$$

This scaling clearly cannot be appropriate in the limit of very small slope, $\theta\to 0$. Moreover, the velocity scale for the flow up and down the slope,

$$\psi_s/H\propto(\cos\theta/\sin^{\frac{1}{2}}\theta)$$

increases without limit while in fact this circulation should vanish as $\theta\to 0$. Thus, in (14) even if ψ were to remain finite as $\theta\to 0$, the second term on the left vanishes more rapidly than the term on the right, and at small slopes the generation of vorticity is primarily the result of buoyancy gradients along the slope with redistribution across the layer by turbulent diffusion. For very small angles, then, the case of our primary interest here, we must have

$$\nu\frac{\psi_s}{H^4}\sim N^2\cos\theta\sin\theta\gg\frac{N^2\sin^2\theta\psi_s}{\kappa}, \tag{18}$$

or that

$$\psi_s\sim\frac{N^2H^4}{\nu}\cos\theta\sin\theta, \tag{19}$$

rather than (17). We note that (19) clearly does not give separate scales for ψ_s and H – other physical considerations will be used to estimate the latter. We note incidentally that ψ_s is very sensitive to H and the second term in the buoyancy flux expression (13) even more so (as H^9!), even though this term will be shown to be negligible as $\theta\to 0$ provided H remains finite. Note also from (13) that, as Garrett (1990) points out, if $\kappa(y)$ decreases rapidly across the boundary layer from its scale value κ (at the boundary, say) then the advective flux represented by the second term in the integral may well be dominant. However, our shadowgraph observations of the boundary layer (a photograph is given in figure 4 of PSS) suggest rather uniform turbulence below a well-defined undulating front. Above this front, fine-scale density structures could be seen in fluid that had detrained and was drifting away in a much more quiescent manner as the structures gradually disappeared. These observations led us to believe that $\kappa(y)$ does not vary rapidly within the active turbulent region. It is also possible, as Woods (1991) has pointed out, that at some

intermediate slopes the balance implied by (15) may be attained, but if the two terms in (12) or (13) are comparable at these slopes, the overall dependence of F_B upon θ may not be simple since the two terms may involve different slope factors.

The physical quantities that are available to us in this problem are the stratification of the fluid, characterized by N, the turbulence characterized by κ (or ν) and the angle of the slope, θ. On dimensional grounds the lengthscale that can be constructed from these is $l_s \sim (\kappa/N)^{\frac{1}{2}} f(\theta)$, which is presumably finite for all values of θ, where $f(\theta)$ must be determined from experiments, for instance. For the case in which turbulence is generated along a flat bottom boundary in a stratified fluid $l_s = (\kappa/N)^{\frac{1}{2}}$ and it is defined as the distance over which buoyancy forces become important. This is the Ozimdov scale, also referred to as the 'overturning' scale (Turner 1979).

In the experiments to be described in the next section, the boundary layer along the sloping boundary was established very rapidly for all slopes as the turbulence was first turned on. This indicated that, initially at least, the thickness of the boundary layer could only depend on N and κ, as for the flat-bottom case, so that H scaled with l_s. In PSS it was shown that at a fixed slope of 9.4° the boundary-layer thickness δ, defined by the average position of the turbulent interface, scaled adequately as $(\kappa/N)^{\frac{1}{2}} \propto (\omega a d/N)^{\frac{1}{2}}$, though the results presented there included the $(\sin\theta)^{-\frac{1}{2}}$ factor suggested by (16), which we have now seen to be untenable in the small-slope limit. Although the thickness of the boundary layer was not measured in such detail as it was in PSS, there was no apparent dependence of δ on the slope over the range 7.1° to 23.5°. Removal of the $(\sin\theta)^{-\frac{1}{2}}$ factor gives

$$\delta = \left\{0.59\left(\frac{\omega a d}{N}\right)^{\frac{1}{2}} + 0.14\right\} \text{cm}. \tag{20}$$

We therefore take the scale depth $H(\propto \delta)$ as

$$H = (\kappa/N)^{\frac{1}{2}}, \tag{21}$$

so that

$$\psi_s = \kappa \cos\theta \sin\theta, \tag{22}$$

where we have reasonably assumed that the turbulent Prandtl number is $O(1)$.

We now return to (9) and use the scales defined above to determine the scale of the buoyancy variation across the boundary layer. We obtain

$$(\Delta B)_s = \frac{N^2 \sin\theta}{\kappa} H\psi_s \tag{23}$$

or using (22)

$$(\Delta B)_s = HN^2 \cos\theta \sin^2\theta. \tag{24}$$

The total buoyancy transport across the level of maximum stratification can be found from (12) or (13). With the scales defined by (21) and (22) or (24), the first (diffusive) term scales as $(\kappa N)^{\frac{3}{2}} \sin\theta$ and the advective term as $(\kappa N)^{\frac{3}{2}} \cos^2\theta \sin^3\theta$; the latter clearly becomes insignificant as $\theta \to 0$.

Consequently in spite of the caveats expressed following (19), the angular dependences alone are sufficient to assure us that for small slopes, the buoyancy transport is mainly due to turbulent dispersion and that the role of the internal circulation is negligible in enhancing the dispersive characteristic of a turbulent boundary layer along a long sloping boundary when the density stratification is linear with depth. The question of whether the slopes used in these experiments are

indeed 'small enough' will be considered at the end of §3 in the light of the magnitudes of the measured fluxes. The inefficiency of the internal circulation in transporting mass at low angles seems to be related to the weakening of the stratification inside the boundary layer due to the mixing process. The reduction in the density gradients is expected when the turbulence is well developed and when the turbulent region is relatively thin, as was the case in the present experiments. The inefficiency of the secondary circulation was first noted by Garrett (1990). Equations (22) and (23) explicitly show that the buoyancy variations across the boundary layer inside the layer are reduced by a factor $\sin^2\theta$ from their scale in the ambient region which is $HN^2\cos\theta$. The advective buoyancy flux will then be reduced accordingly. However, as Garrett (1990) and Woods (1991) point out, there may exist a range of larger angles of bottom slopes for which the advective flux may make a significant contribution to the total flux of buoyancy if the numerical values of $\psi(y)/\psi_s$ in (13) are not too small.

The total buoyancy transport can be specified in terms of an overall dispersion coefficient K_x as

$$F_B = -K_x \delta \frac{\partial B}{\partial x} = -K_x \delta N^2 \sin\theta, \tag{25}$$

and from (12) or (13)

$$K_x \approx \kappa, \tag{26}$$

the average of the diffusivity $\kappa(y)$ across the boundary layer, when the advective contribution is neglected, as is certainly appropriate at small slopes.

As mentioned previously, when the stratification in the ambient fluid extends only over a limited region, in addition to the internal streaming motion there is the overall convergence in the boundary layer produced by the diffusion of buoyancy somewhat above and below the ambient pycnocline, leading to intrusion of fluid into it. We want to consider next the volume fluxes associated with this component of the flow. When N is locally constant everywhere the turbulent fluxes $\overline{b'v'}$ vanish both at $y = 0$ and $y = \delta(\propto H)$, so that the mean volume transport defined by

$$F_v = \int_0^\delta u \, \mathrm{d}y \tag{27}$$

vanishes. Experiments using a non-uniform density stratification confirmed that the net volume flux in the boundary layer vanished at the level where $\partial N/\partial Z = 0$, hereafter denoted by Z_0. Thus, as stated in PSS, the existence of a local region over which $N \approx$ constant still results in the presence of a level at which the volume flux vanishes and, to first approximation, the scaling arguments of the present section hold.

If u_c represents the velocity scale of the convergence motion (at the edge of the pycnocline) then the overall diffusion of buoyancy outwards balances the convergence inwards. Over the timescales that characterize the turbulence the mean buoyancy distribution is quasi-stationary and can be described appropriately by

$$u_c \frac{\partial \bar{B}}{\partial x} \approx K_x \frac{\partial^2 \bar{B}}{\partial x^2}. \tag{28}$$

We note that in (28) the possible effects of the secondary circulation on the overall convergence are included in K_x. We also note that when $N^2(Z)$ can be approximated by a Gaussian function (cf. §3) then the solution for u_c is approximately a linear

function of the distance along the slope, x. This is in agreement with the experimental results shown in figure 11 and discussed below.

We can use (28) to obtain the scale for u_c as

$$u_c \sim K_x/L, \tag{29}$$

where $L \sim h/\sin\theta$ and K_x is given by (25). The volume transport associated with the convergent flow, from (27) is then

$$F_v \approx u_c \delta \sim K_x \frac{H}{L} \sim K_x \frac{H \sin\theta}{h}, \tag{30}$$

or using (21) and (26)

$$F_v \sim \frac{\kappa^{\frac{3}{2}}}{N^{\frac{1}{2}} h} \sin\theta, \tag{31}$$

for small angles.

We finally note *a posteriori* that the terms that were neglected in the boundary-layer type of approximation to the vorticity equation (4), mainly the advection of vorticity and the diffusion of vorticity up and down the slope, are either of $O(\sin^3\theta)$ or of $O(\sin^5\theta)$. These are to be compared with the terms that were kept which are of $O(\sin\theta)$.

3. Laboratory experiments and results

3.1. *Experiments*

The experiments were conducted in the rectangular tank made of glass walls framed in metal and mounted on a horizontal table used by PSS in the original experiments with a bed slope of 9.4° (hereinafter referred to as θ_0). Details of the experimental setting, instruments and measuring techniques can be found in PSS. Here we summarize the experimental work and describe the new observations and results. The tank was found appropriate to run experiments with slopes of $\theta_1 = 7.1°$, $\theta_2 = 16.35°$ and $\theta_3 = 23.5°$, where the angle θ is defined by the inclination of the sloping boundary to the horizontal. Variation in the slope was achieved by rebuilding the rigid ramp that provided support for the sloping bed, by constructing a new oscillating bed and by realigning the motor and drive system for each angle. We would have liked to make measurements at even smaller angles than 7.1° to be sure that the slopes were indeed in the range consistent with the small-slope approximation, but the restricted length of the tank and the need to maintain an adequate depth precluded this. As in the original experiments, the fluid system consisted of two layers, one of fresh water and the other of a salt solution of known density, the two being separated by the slowly evolving pycnocline. The turbulent boundary layer was created along the sloping boundary of the tank by oscillating a rough mat in the direction of the slope. For each experiment, the slope and the amplitude and frequency of the oscillation were kept constant while the evolving ambient density field was monitored by measuring the temporal development of its variations with depth at a fixed location with a conductivity probe.

The general characteristics of the mean circulations observed were essentially the same for all slopes considered in this study. After the oscillation of the rough mat had started, the turbulent boundary layer developed within a few seconds. The intrusion of well-mixed boundary fluid into the interior regions at the level of the pycnocline

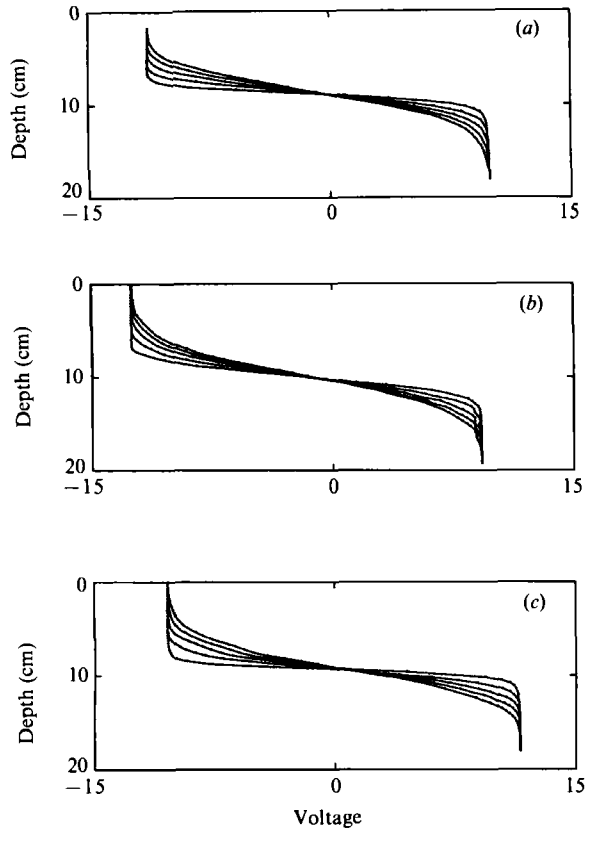

FIGURE 3. Representative sets of profiles redrawn after digitization from the chart recorder. Increasing voltage indicates increasing density. The sets correspond to: (*a*) experiment 3 with θ_1 (*b*) experiment 10 with θ_2 and (*c*) experiment 6 with θ_3.

was also set up rapidly and continued steadily throughout, as well as the entrainment of lower and upper unstratified fluid from the interior into the boundary layer. The experiments were concluded when either the density of the initially fresh water at the top of the tank or the density of the most saline water at the bottom began to increase or decrease respectively from their initial values. The total time elapsed varied for each set of experiments with the different slopes and within each set also, according to changes in the combination of frequency and amplitude of the oscillations. On the average, the total time for each experiment ranged between 30 and 90 min.

The conductivity probe was mounted on a movable carriage enabling its positioning at any point along the tank. The density measurements were recorded on an (x, y) flat-bed plotter. A typical set of profiles obtained from the chart recorder in a single experiment is shown in figure 3, for each angle. Probe traverses made at different horizontal locations confirmed that at any instant the distributions depicted in figure 3 were basically the same along the whole tank so that the density field in the interior fluid was a function of the vertical coordinate only.

Qualitative observations of the mixing processes and circulation patterns were made by injection of various dyes, and the structure of the boundary layer and the surrounding regions were observed by means of shadowgraph images. Dye studies inside the boundary layer of the same type described in PSS confirmed the existence

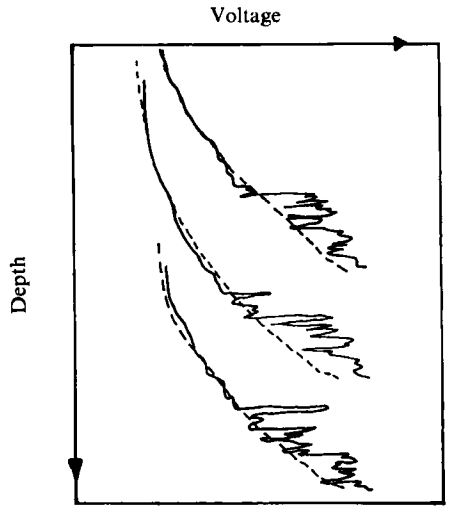

FIGURE 4. Typical density profiles from probe traverses into the turbulent boundary layer.

of the internal circulation and the subsequent intrusion of mixed fluid into the ambient regions for all the slopes considered here. At the start of an experimental run, two dyes of different colour were used and one was placed very near the oscillating mat and the other at some distance from it. This enabled us to observe that the fluid near the mat was less dense than the outside fluid at the same level, hence moved upwards, while that near the outer edge of the boundary layer was heavier than its surroundings and tended to move downwards. The single intrusion flow pattern was a prominent feature of the interior flow of all the experiments conducted in this study.

In the experiments reported by Ivey & Corcos (1982), with a turbulent boundary layer along the vertical end of a tank and with an initial linear ambient stratification, a multiple intrusion pattern characterized the flow in the interior. In the case of an initial two-layer stratification, the authors also reported that the initial stage of the intrusion of fluid from the boundary layer was of the single jet type that broke up into weaker intrusions rapidly, the multiple intrusions appearing below and above the level of the initial interface separating the fluids of different densities; the more remote the intrusion from the interface the later it appeared. Our observations indicated that for the largest slope angle the tendency was for the intrusive layer to be initially wider under similar conditions of thin pycnocline and other laboratory parameters but additional smaller-scale intrusions were not evident. Even when the initial stratification was not as sharp, though of the same order of the reported values of Ivey & Corcos, the single intrusion jet type was clearly observed, its shape remaining fairly constant throughout time.

The average thickness of the turbulent boundary layer achieved in these experiments was of the order of 2 cm or less, which made it mechanically difficult to measure the mean density field there. As in the initial experiments of PSS, several traverses inside the boundary layer were conducted to confirm the observations from dye studies of the internal mean circulation. A set of typical boundary-layer density profiles is depicted in figure 4, and while they were not used in a more quantitative analysis they show that the fluid at the outer edge of the boundary layer is denser than the ambient fluid at the same level. Probe traverses in the boundary layer

performed at different levels of the ambient pycnocline region also showed that the profiles tended to correspond to well-mixed conditions in the normal direction at about mid-depths in the pycnocline and that the difference between mean densities inside and outside the boundary layer, although significant, was small when compared with the range of buoyancy in the fluid as a whole.

It was noted that the density profiles corresponding to an initially sharper pycnocline had a gradient that decreased more rapidly with time near the start than those for which the initial stratification was weaker. A similar observation was reported by Ivey & Corcos (1982). In their few experiments with a two-layer fluid system, the approximately linear central part of the density field had a gradient that became weaker more rapidly with time than that which evolved from an initially uniform stratification.

The vigorous turbulent mixing was confined to the boundary layer along the sloping bottom, the edge of which remained sharp over the region of significant stratification. The stratified region inside the boundary layer extended beyond the corresponding stratified depth in the interior, and its extent in the slope direction increased slowly with time as turbulent mixing brought denser fluid upward. Hence, as expected, away from the region of the pycnocline the thickness of the boundary layer began to increase, becoming a weak function of distance along the slope. The characteristic timescale of this change, as well as the change in the width of the intrusion, was larger than both the internal boundary-layer timescale and the timescale of the ambient density evolution.

The dependence of H on the slope angle was not measured directly in the present work, where the range of the monitored values of boundary-layer thickness were between 1 and 2 cm, as in the work of PSS, depending essentially on the intensity of the stirring and the stratification, and the differences, when detectable, were well within the scatter in the results reported originally. To the accuracy of the experiments, the dependence of the thickness of the boundary layer on the slope of the bottom boundary, for the range of angles used, was not significant and it was the combined effects of the oscillation of the rough surface and the stratification in the ambient fluid that controlled the boundary-layer thickness. If the boundary-layer thickness had scaled according to (16) it would have varied by a factor of about 2 between the smallest and largest angles, and this was not observed. This fact, in turn, lends support to the revised scale for H given in (21).

Dye traces in the ambient regions confirmed that the slow interior motion in the stratified layer was basically horizontal. The horizontal velocity at a given depth essentially varied linearly with horizontal distance, and the vertical velocities were very small and independent of horizontal position except in the very narrow top and bottom layers. The isopycnals remained horizontal as they spread vertically in response to the intrusions, while the isopycnal surface initially at height Z_0 remained there throughout an entire experiment (see figure 3, where all profiles pass through the same point in the interior; there the density gradient had a maximum). At this height, consequently, the net volume flux in the boundary layer vanished.

3.2. *Analysis of results*

Twenty-eight experimental runs were carried out to completion; eleven with $\theta_1 = 7.1°$, ten with $\theta_2 = 16.35°$ and seven with $\theta_3 = 23.5°$. Some experiments were mainly devoted to determining the reliability of the instruments. Satisfactory series of profiles were obtained in seven, eight and six runs, respectively, and the pertinent operating parameters are specified in tables 1, 2 and 3. Between thirty-five and forty

Experiment number	Frequency ω (rad/s)	Amplitude a (cm)	Range of N_{max} (rad/s)	Initial density top (g/cc)	Initial density bottom (g/cc)
1 (*a*)	14.68	0.262	6.13–4.59	0.999	1.058
1 (*b*)	20.77	0.262	4.59–3.95	0.999	1.058
2	20.10	0.414	6.38–3.43	0.998	1.058
3	25.94	0.409	5.94–3.39	0.998	1.057
4	15.17	0.400	5.87–3.63	0.999	1.059
5 (*a*)	42.59	0.254	6.17–4.08	0.998	1.060
5 (*b*)	46.65	0.254	4.08–3.28	0.998	1.060
6	42.22	0.475	6.34–3.55	0.999	1.060
7 (*a*)	29.46	0.414	6.12–4.62	0.999	1.064
7 (*b*)	41.32	0.414	4.62–3.46	0.999	1.064

TABLE 1. Operating parameters for experiments with $\theta_1 = 7.10°$. Position of probe along the tank: 51.0 cm

Experiment number	Frequency ω (rad/s)	Amplitude a (cm)	Range of N_{max} (rad/s)	Initial density top (g/cc)	Initial density bottom (g/cc)
(*a*) 1	15.12	0.377	5.60–3.76	0.999	1.065
2	24.44	0.379	4.19–3.03	0.999	1.062
3	37.88	0.278	4.89–3.17	0.999	1.063
4	30.39	0.225	5.84–3.85	1.000	1.063
(*b*) 5	31.40	0.232	5.19–3.83	0.999	1.059
6	31.44	0.235	6.44–4.02	0.999	1.059
7	31.74	0.232	5.08–3.45	0.999	1.059
10	23.90	0.507	4.66–3.22	0.999	1.058

TABLE 2. Operating parameters for experiments with $\theta_2 = 16.35°$. (*a*) Position of probe along the tank: 84.7 cm, (*b*) 127.0 cm

Experiment number	Frequency ω (rad/s)	Amplitude a (cm)	Range of N_{max} (rad/s)	Initial density top (g.cc)	Initial density bottom (g/cc)
1	23.78	0.395	6.16–3.56	0.999	1.059
2	23.84	0.258	6.40–3.45	0.999	1.058
3	31.46	0.234	6.93–3.77	0.999	1.058
4	11.90	0.390	6.31–3.84	0.999	1.059
5	15.71	0.391	6.92–3.66	0.999	1.060
6	23.50	0.501	5.95–3.02	0.999	1.046

TABLE 3. Operating parameters for experiments with $\theta_3 = 23.5°$. Position of probe along the tank: 150.0 cm

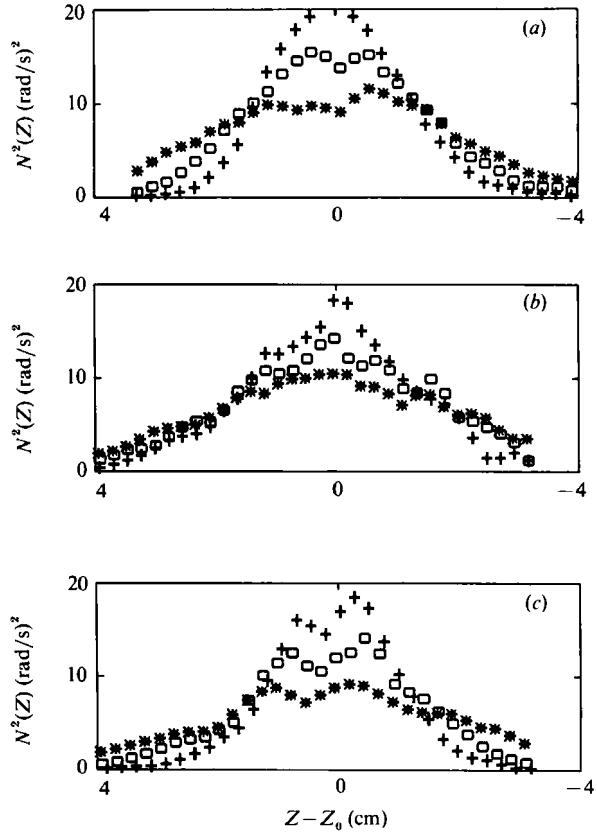

FIGURE 5. Typical profiles of $N^2(Z)$ taken at three different times throughout an experiment; the maximum of the curves decreases with time. Data correspond to: (*a*) experiment 3 with $\theta_1 = 7.1°$, (*b*) experiment 10 with $\theta_2 = 16.35°$, (*c*) experiment 6 with $\theta_3 = 23.5°$.

profiles for each angle were analysed in detail. For each fixed angle, the ambient stability frequency N, and the frequency ω and amplitude of the oscillating mat a, were varied from experiment to experiment. The need to preserve the values of these parameters used in the experiments with the slope of 9.4°, and hence isolate the angle dependence, and limitations imposed by the existing equipment imposed constraints on the range of parameters actually used in the experiments. Enough data were gathered in the present experiments, however, to provide a fairly good base for comparison with the experiments at 9.4° and, in addition, to extend the range of the values of ω and a to lower numbers, also with enough data so that intercomparisons within the new set are possible. At the lowest values of the product ωa, viscous effects in the boundary layer became important, rendering the mean internal circulation inefficient. To avoid the influence of viscosity, the minimum Reynolds number of the turbulent fluctuations in the boundary layer ($=\omega a d/\nu$) that we considered acceptable was approximately 400. Results from these experiments with a lower value were mostly omitted from the data analysis.

Measurements of the ambient density field were digitized in two manners: at equal intervals of depth with $\Delta Z = 3$ mm in the graph paper; and at equal intervals of voltage corresponding to a displacement of 3 mm in horizontal distance on the recorder. This yielded data for density as a function of depth and time, $\rho(Z, t)$, where Z is the vertical coordinate in the tank positive upwards, and data for the height of

the density surfaces as a function of density and time $\xi(\rho, t)$, respectively. From the first set of data the density gradient $\partial\rho(Z)/\partial Z$, the stability frequency $N(Z)$ and the mass flux were computed as functions of depth Z for each profile. The derivative of the density field was approximated by a centred finite-difference expression, and in all cases time differences were replaced by the measured time interval between probe traverses. Throughout these experiments with an initially thin pycnocline, for all different slopes the distributions of $N^2(Z)$ remained approximately Gaussian. Figure 5 shows typical profiles of $N^2(Z)$ for each slope value at three different times: the initial distribution; midway through an experimental run; and at the final time, shortly before the experiment was ended. The profiles shown correspond to runs with different slopes with all other laboratory parameters closely equal.

The measurements and direct computations refer to quantities in the ambient fluid. Our interest, however, is focused on the transports associated with the circulation observed inside the boundary layer and we can use the measurements to obtain estimates of these transports. The arguments that allow us to relate the ambient measurements with boundary-layer transports are those used in the original experiments of PSS and summarized here. The volume flux in the boundary layer was obtained from application of the incompressibility condition. The total volume flux across a horizontal surface at any level Z vanishes, so that the boundary-layer volume flux is equal but opposite to that in the interior

$$F_v = -\int_{\text{int}} W \, \mathrm{d}X, \tag{32}$$

where W is the vertical component of the interior velocity field and X the horizontal coordinate, measured from the vertical end of the tank. The interior region is non-turbulent and can be regarded as non-diffusive so that the vertical velocity there is simply the rate of rise of an isopycnal, $\dot{\xi}(\rho(X))$, measured as described above.

The boundary-layer buoyancy flux can be expressed in terms of quantities measured in the interior by integration of the mean buoyancy equation throughout the region $A(Z)$ of the tank above the level Z, schematically

$$\frac{\partial}{\partial t}\int_{A(Z)} B(Z,t)\,\mathrm{d}A = \int_{\text{int}} B(Z,t)\,W\,\mathrm{d}X + \int_{\text{b.l.}} (uB(Z,t)+D_B)\,\mathrm{d}y/\sin\theta, \tag{33}$$

the first term on the right representing the upwards transport in the interior associated with the vertical motion there and the second the advection and diffusion transports in the boundary layer. Thus the net boundary-layer transport of buoyancy is

$$F_B(Z,t) = \frac{\partial}{\partial t}\int_{A(Z)} B(Z,t)\,\mathrm{d}A - W(Z)\,B(z,t)\,L(Z), \tag{34}$$

the integral term being found from the change in the buoyancy field above Z between successive traverses. In particular, at the level Z_0 where $W(Z_0) = 0$ and the boundary-layer volume flux vanishes, the boundary-layer buoyancy transport is entirely the result of turbulent dispersion so that

$$F_B(Z_0) = \frac{\partial}{\partial t}\int_{A(Z_0)} B(Z,t)\,\mathrm{d}A. \tag{35}$$

The volume transport was computed from measurements of the vertical displacements of isopycnals between successive probe traverses, as mentioned above

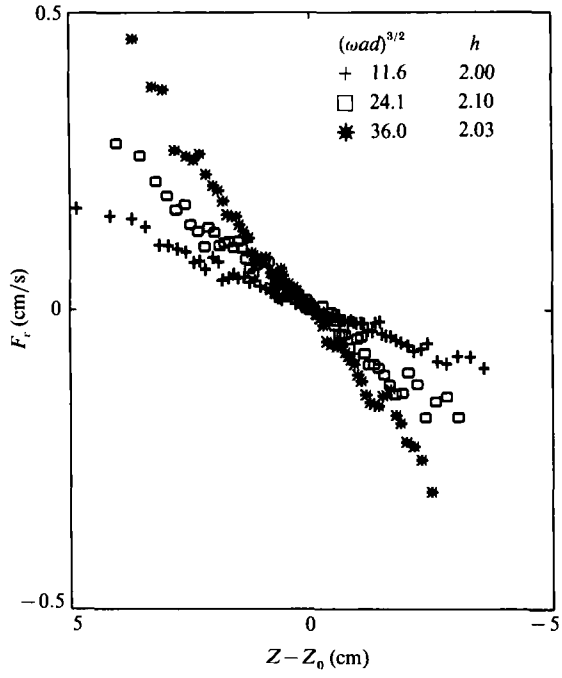

FIGURE 6. Three unscaled measurements of volume transport profiles performed with $\theta_1 = 16.35°$. Data correspond to: +, experiment 1, profile 5; □, experiment 2, profile 3; ✱, experiment 10, profile 2.

and detailed in PSS. An example of typical profiles of computed volume fluxes is shown in figure 6. For the slope, $\theta_2 = 16.35°$, the data are from single measurements at about the same time in three different experiments corresponding to three different values of ωa. The boundary-layer volume transport in the direction of the slope decreases in magnitude with distance, vanishes at the level Z_0 and increases farther along the slope. The figure indicates a linear dependence, and that the curves with steeper slopes correspond to higher values of ωa.

The buoyancy transport was calculated from the measurements as detailed in PSS. Figure 7 shows a summary of the normalized distributions of total buoyancy transport with $(Z-Z_0)/h$ for each of the three slopes used in these experiments, where h is the half-thickness of the pycnocline. These data represent the contribution from turbulent diffusion in the boundary layer, as described above. The downward transport of buoyancy due to turbulent diffusion increases with depth to a maximum at the level Z_0 and decreases below that level, as does the vertical gradient of buoyancy. Away from the pycnocline region this transport vanishes. The scatter of the data below the pycnocline indicates a weak buoyancy transport there, which was associated with the presence of large, slow eddies in the lower unstratified region of the tank. These eddies were due to the extension of the oscillating mat slightly beyond the end of the ramp. We note that the weak slope dependence is apparent from the data used in figure 7, since the envelopes in these figures are similar to each other although they correspond to data from different slopes.

The mean distribution with depth of the total buoyancy transport in the boundary layer can be represented as the sum of the diffusive and convective components, as indicated by (34). The data yield similar plots (not shown) to that depicted in figure 17 in PSS.

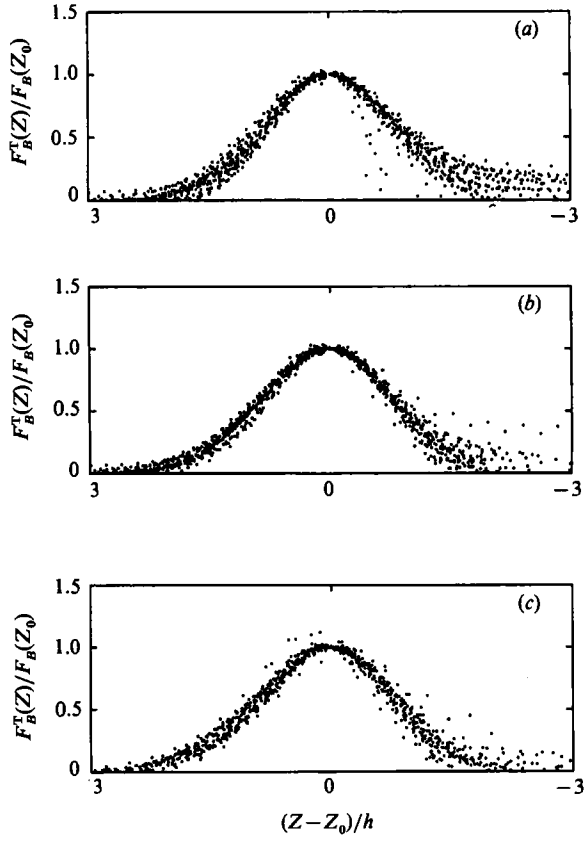

FIGURE 7. A summary of the mean distribution of the total rate of change of buoyancy in the area of the tank above Z_0 for the three different slopes of the bottom boundary layer: (*a*) $\theta_1 = 7.1°$, (*b*) $\theta_2 = 16.35°$ and (*c*) $\theta_3 = 23.5°$. These sets represent the contribution to the mean buoyancy transport from turbulent dispersion in the boundary layer.

3.3. *Transports and boundary-layer parameters*

As in PSS, we measure the local dispersive characteristics of the turbulence in terms of the laboratory parameters and express the relations between buoyancy and volume transports and the experimental quantities using scaling relations obtained from a model for the flow.

The relation between the overall diffusive transport in the boundary layer and quantities measured in the laboratory experiments essentially expresses that

$$F_B(Z_0) \propto -[\omega a d N(Z_0)]^{\frac{3}{2}}, \tag{36}$$

where Z_0 is the level at which the volume flux vanishes and where the total transport of buoyancy is entirely due to turbulent dispersion. Data from measurements of the density field in the interior at the level Z_0 were used to compute the mass flux according to (35) and plotted against laboratory parameters as indicated by (36). Details of this calculation can be found in PSS. The values of $N(Z_0)$ were also determined as indicated in PSS. Results from these calculations were plotted and least-squares fits to the points were used to obtain the values of the coefficients for

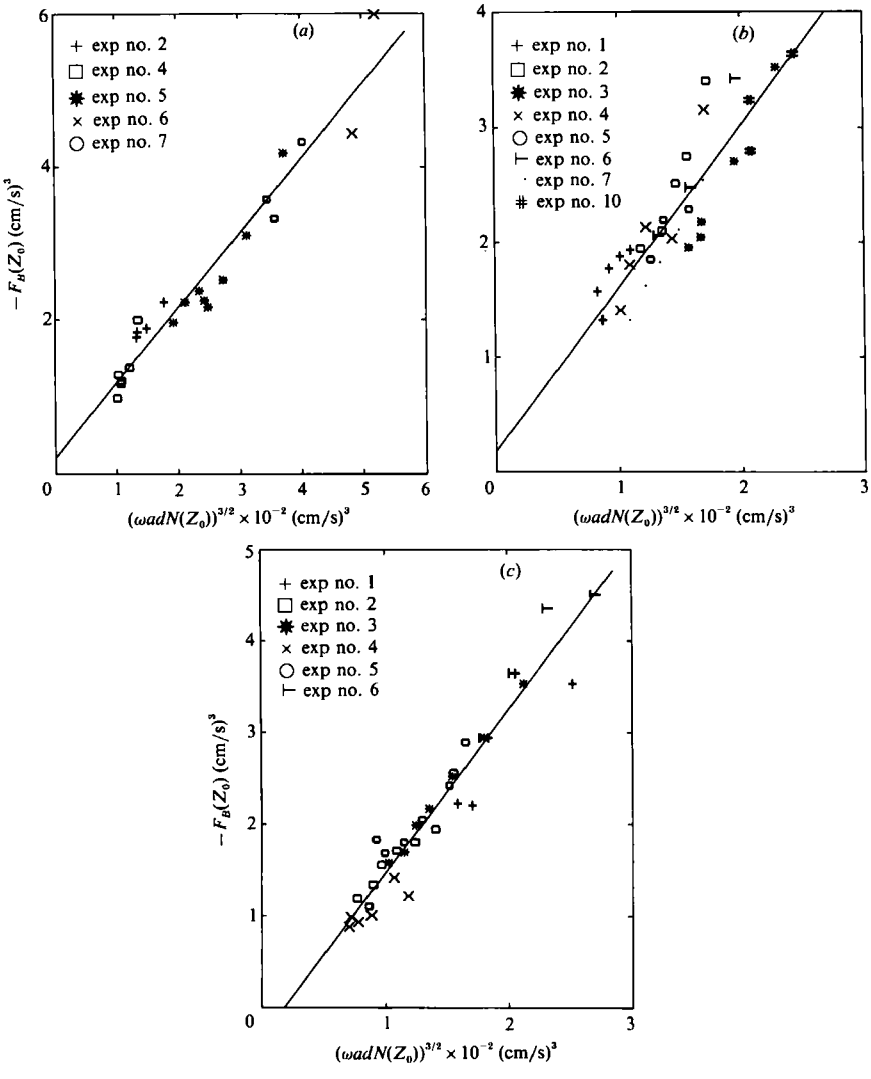

FIGURE 8. Measurements of the buoyancy transports across the height Z_0 scaled according to (36) in §3.3, with (*a*) $\theta_1 = 7.1°$, (*b*) $\theta_2 = 16.35°$ and (*c*) $\theta_3 = 23.5°$.

the linear relation. These results are shown in figure 8(*a–c*) for each angle studied in the present work.

A least-squares fit to the data yielded the following lines (also shown in the figures):

$$\left.\begin{aligned} F_B(Z_0) &= -0.97 \times 10^{-2}[\omega adN(Z_0)]^{\frac{3}{2}}, \quad \theta_1 = 7.1°, \\ F_B(Z_0) &= -1.42 \times 10^{-2}[\omega adN(Z_0)]^{\frac{3}{2}}, \quad \theta_2 = 16.35°, \\ F_B(Z_0) &= -1.78 \times 10^{-2}[\omega adN(Z_0)]^{\frac{3}{2}}, \quad \theta_3 = 23.5°, \end{aligned}\right\} \tag{37}$$

respectively, with a standard deviation about the lines in all cases of order 10^{-1}. A close examination showed that the data from some individual experiments did not follow the overall trend of the whole data set in each figure, except perhaps for the data in figure 8(*c*) corresponding to the largest slope $\theta_3 = 23.5°$. This departure was

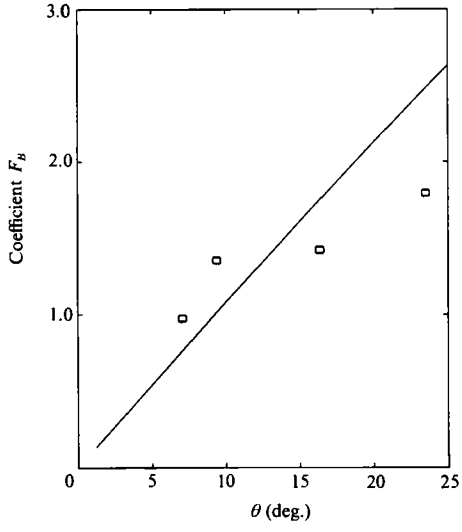

FIGURE 9. A summary of predicted (——) and experimental (□) coefficients as a function of bottom slope.

most prominent for the smallest slope $\theta_1 = 7.1°$ (see figure 8*a*). From the data summarized in tables 1–3, we note the relationship between these departures and the smallness of the values of ωa, i.e. when viscous effects became important. The larger errors in these measurements were mainly related to two factors: the determination of the frequency of the oscillating mat and the viscous effects at low Reynolds numbers, these effects being more pronounced at low angles.

The numerical coefficients above, expressing the dependence on the slope angle, are plotted in figure 9, together with the value 1.35×10^{-1} at $\theta_0 = 9.4°$ from PSS. It is clear that the buoyancy transport increases with slope over this range. The scaling given here predicts the dependence as $\sin\theta$ and although the agreement with these limited data is only fair, it is certainly consistent with a monotonic increase. In the figure, the solid line corresponds to a linear regression fit using the present prediction (i.e. $\sin\theta$). One can see by eye that a better empirical fit might be something like $(\sin\theta)^{\frac{1}{2}}$, but unfortunately, we are unable to provide any reasonable basis for this. Such a dependence would be found if δ were proportional to $(\sin\theta)^{-\frac{1}{2}}$, but the only justification for this is the PSS scaling which, as we have seen, is untenable at small angles. If $\sin\theta$ factors are restored to the expressions in (37), the numerical coefficients average to 0.064, so that

$$F_B(Z_0) = -0.064 \times [\omega a d N_0(Z_0)]^{\frac{3}{2}} \sin\theta. \tag{38}$$

Now, from (25) and (26), $F_B = \kappa\delta N^2 \sin\theta$ at small angles, where $\delta = 0.6(\omega a d/N)^{\frac{1}{2}}$, which by comparison with (38) indicates that $\kappa \approx 10^{-1}(\omega a d)$, which seems a very reasonable value. Our observations of the shadowgraph images confirmed that the size of the largest eddies was approximately equal to d (the spacing of the roughness elements) and their velocity must scale as ωa, the maximum speed in oscillations, though fluid velocities themselves were an order of magnitude smaller than this. Consequently, the numerical coefficient in κ that one would expect is closer to that found. Since $\omega a d \approx 10\kappa$, the boundary-layer thickness $\delta \approx 2(\kappa/N)^{\frac{1}{2}}$ and (38) can be written as

$$F_B(Z_0) = -2.0 \times [\kappa N_0(Z_0)]^{\frac{3}{2}} \sin\theta. \tag{39}$$

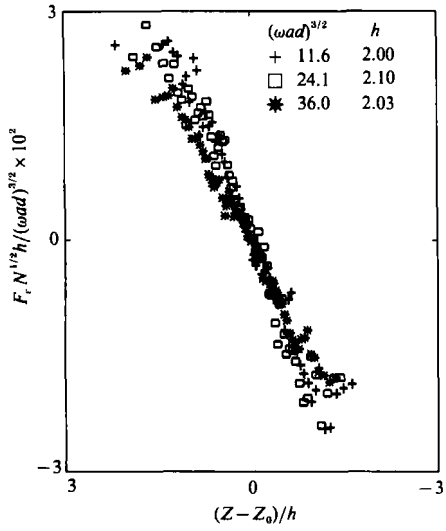

FIGURE 10. The same profiles as in figure 6 for volume transport measurements, scaled according to (40) in §3.

This empirical coefficient is then determined to about 11–17% uncertainty, still within the bounds of experimental error.

For the volume fluxes associated with the mean overall convergence the assumption of a quasi-stationary balance between the net turbulent dispersion along the slope and the overall convergence led to a linear relation between the scaled volume fluxes and depth, over the depth range of significant stratification, expressed as (cf. (31))

$$\frac{F_v N^{\frac{1}{2}} h}{(\omega ad)^{\frac{3}{2}}} \propto \frac{Z-Z_0}{h}, \tag{40}$$

for each of the angles of the sloping boundary. In the plot of figure 6, the linearity between computed volume fluxes and depth was already apparent. When the same profiles were scaled according to (40) and plotted against the normalized vertical coordinate $(Z-Z_0)/h$, figure 10, the data collapsed about a straight line confirming this linearity, much as was the case with data obtained with θ_0 (cf. figures 11 and 12 in PSS). The collapse of all the data gathered in these experiments about a straight line for each individual angle yielded empirical coefficients that followed the same pattern as the coefficients for the buoyancy transport; i.e. they increase with the angle of the slope. These data were plotted in the same manner as figure 10 and are shown in figure 11 (*a–c*). Since the volume flux must vanish at the top and bottom of the tank, away from the region significantly stratified, i.e. as $|Z-Z_0|/h$ increases, the linear relations break down as can be seen in the figures for values of $|Z-Z_0|/h$ larger than about 1.0–1.5. The data show the same scatter away from the regions of significant stratification as expected, since there the displacements of the isopycnals are harder to measure.

The constants of proportionality between the scaled volume transport and $(Z-Z_0)/h$ obtained from a least-squares fit of all the data for each angle in figure 11 were: 1.2×10^{-2}, 1.7×10^{-2} and 1.5×10^{-2} for θ_1, θ_2 and θ_3 respectively. The coefficient for data using θ_3 is slightly smaller than expected and this may be due to the larger scatter in the data shown in figure 11 (*c*) away from the centre regions of the pycnocline. This scatter follows the same characteristics described above but it is

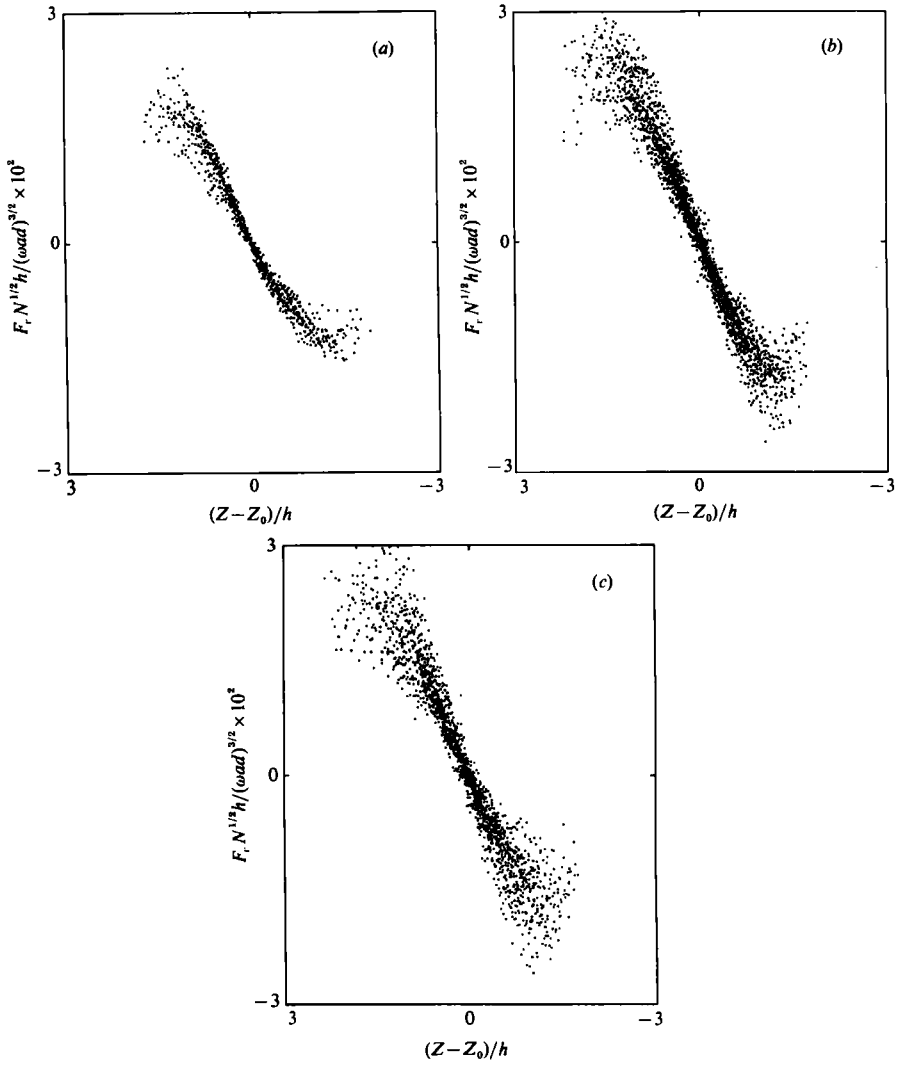

FIGURE 11. A summary diagram of the scaled volume fluxes in all sets of experiments at (*a*) $\theta_1 = 7.1°$, (*b*) $\theta_2 = 16.35°$ and (*c*) $\theta_3 = 23.5°$.

further accentuated in this case by the effects of viscosity at low Reynolds numbers. In this figure all data obtained from experiments with θ_3 are included and we can see from table 3 that some experimental runs were conducted at low values of ωa. A line obtained ignoring these data would have a slightly steeper slope, thus yielding a larger numerical coefficient more in agreement with the slope dependence described by (31).

When we restore the slope factors to these lines and use the estimate for κ in terms of $\omega a d$ we obtain the values of 3.0, 1.8 and 1.2 for θ_1, θ_2 and θ_3 respectively. We use the data of PSS for θ_0 to obtain a coefficient of 1.8. These values yield an averaged numerical coefficient of 2.0, so that we may write a general relation for the volume flux as

$$F_v(Z) = 2.0 \times \frac{\kappa^{\frac{3}{2}}}{N^{\frac{1}{2}} h} \sin\theta \left(\frac{Z-Z_0}{h}\right). \tag{41}$$

A final note on the numerical coefficients seems pertinent. The average final numerical constant is obtained assuming that the contribution of the secondary circulation to the buoyancy and volume transports is negligible, which we have shown to be the case for small angles. From the data for the buoyancy flux we note that the empirical coefficients for the two smallest angles would yield an average of about 2.5, somewhat larger than an average with those for the two largest angles which would be about 1.5. This may be due to possible effects of the secondary circulation on the dispersive characteristics of the boundary layer, although more measurements would be necessary to be more conclusive.

The magnitudes of the fluxes measured do allow us to check *a posteriori* whether the bottom slopes used in these experiments were indeed small enough to satisfy the inequality expressed in (18). It was found that for the angles of 7.1° and 9.4°, the third term was 4–5% of the second, rising to 11% at 16.35° and 20% at 23.5°. The last case is clearly marginal and indeed this scaling is least successful for it. Nonetheless, within the uncertainties in these experiments, we believe that the data can be adequately explained by the revised slope dependence in the limit of small slopes presented in this work.

4. Summary and conclusions

The experiments presented here are the continuation and conclusion of those performed by Phillips *et al.* (1986). Here the focus was on the previously unexplored influence of the bottom slope on the boundary-mixing problem and the subsequent intrusion of mixed fluid into the ambient stratified fluid. The general flow patterns observed by PSS at an angle of 9.4° persist over the range of bottom slopes from 7.1° to 23.5° that were accessible to us, and it was found that both the buoyancy and volume fluxes in the boundary layer increase with increasing slope. This is contrary to the slope dependence suggested (but not tested) by PSS and indicates that the boundary buoyancy flux in particular is dominated at these low angles by the longitudinal turbulent dispersion in the boundary layer rather than the advection by the internal countercurrent. A revised scaling of the dependence on bottom slope expressed in (21) and (22) is generally consistent with these new experimental results.

We are grateful to Dr Chris Garrett and two anonymous reviewers for their trenchant and constructive criticisms of the original manuscript, and to the National Science Foundation for the support of the experiments under grant OCE 8613426.

REFERENCES

ARMI, L. 1978 Some evidence for boundary mixing in the deep ocean. *J. Geophys. Res.* **83**, 1971–1979.

CACCHIONE, D. & WUNSCH, C. 1974 Experimental study of waves over a slope. *J. Fluid Mech.* **66**, 223–229.

CALDWELL, D. R., BRUBAKER, J. M. & NEAL, V. T. 1978 Thermal microstructure on a lake slope. *Limnol. Oceanogr.* **23**, 372–374.

ERIKSEN, C. C. 1985 Implications of ocean bottom reflection for internal wave spectra and mixing. *J. Phys. Oceanogr.* **15**, 1145–1156.

GARRETT, C. 1979 Mixing in the ocean interior. *Dyn. Atmos. Ocean.* **3**, 239–265.

GARRETT, C. 1990 The role of the secondary circulation in boundary mixing. *J. Geophys. Res.* **95**, 3181–3188.

GARRETT, C. 1991 Marginal mixing theories. *Atmos. Ocean.* **29**, 313–339.

GREGG, M. C. & SANFORD, T. B. 1980 Signatures of mixing from the Bermuda slope, the Sargasso Sea and the Gulf Stream. *J. Phys. Oceanogr.* **10**, 105–127.

IVEY, G. N. 1987 Boundary mixing in a rotating, stratified fluid. *J. Fluid Mech.* **183**, 25–44.

IVEY, G. N. & CORCOS, G. M. 1982 Boundary mixing in a stratified fluid. *J. Fluid Mech.* **121**, 1–26.

IVEY, G. N. & NOKES, R. I. 1989 Vertical mixing due to the breaking of critical internal waves on sloping boundaries. *J. Fluid Mech.* **204**, 479–500.

MARMORINO, G. O., DANOS, S. C. & MAKI, J. S. 1980 Temperature fine structure of Lake Michigan hypolimnion. *Limnol. Oceanogr.* **25**, 680–699.

MUNK, W. 1966 Abyssal recipes. *Deep-Sea Res.* **13**, 107–175.

PHILLIPS, O. M. 1970 On flows induced by diffusion in a stably stratified fluid. *Deep-Sea Res.* **17**, 435–443.

PHILLIPS, O. M., SHYU, J.-H. & SALMUN, H. 1986 An experiment on boundary mixing: mean circulation and transport rates. *J. Fluid Mech.* **173**, 473–499 (referred to herein as PSS).

STIGEBRANT, A. 1976 Vertical diffusion driven by internal waves in a sill fjord. *J. Phys. Oceanogr.* **6**, 486–495.

THORPE, S. A. 1982 On the layers produced by rapidly oscillating a vertical grid in a uniform stratified fluid. *J. Fluid Mech.* **124**, 391–409.

THORPE, S. A. 1987 Current and temperature variability on the continental slope. *Philos. Trans. R. Soc. Lond.* A **323**, 471–517.

TURNER, J. S. 1979 *Buoyancy Effects in Fluids*. Cambridge University Press. 368 pp.

WOODS, A. W. 1991 Boundary-driven mixing. *J. Fluid Mech.* **226**, 625–654.

WUNSCH, C. 1972 Temperature microstructure on the Bermuda Slope with application to the mean flow. *Tellus* **24**, 350–367.